Genome-wide consensus transcriptional signatures identify synaptic pruning linking Alzheimer's disease and epilepsy

Huihong Li[1,2,3,4], Zhiran Xie[4], Yuxuan Tian[4], Yaxi Yang[4], Bingying Lin[1,2,3,5], Si Chen[1,2,3,5], Jianwei Li[1,2,3,5], Jie Wu[1,2,3], Mingjie Chen[6], Xueke Liu[6], Yushan Sun[6], Zihan Deng[1,2,3,5], Mengqi Hong[1,2,3,5], Bing Huang[1,2,3,5], Naili Wei[1], Xiaoyu Ji[1,2,3,5*]

[1]Department of Neurosurgery, The First Affiliated Hospital of Shantou University Medical College, Shantou, Guangdong 515041, China

[2]Brain Function and Disease Laboratory, Shantou University Medical College, Shantou, Guangdong 515041, China

[3]Department of Pharmacology, Shantou University Medical College, Shantou, Guangdong 515041, China

[4]Program in Computational Biology and Biomedical Informatics, Yale University, New Haven, Connecticut, United States of America

[5]Pain and Related Diseases Research Laboratory, Shantou University Medical College, Shantou, Guangdong 515041, China

[6]Department of Biotechnology and Food Engineering, Guangdong Technion – Israel Institute of Technology, Shantou, Guangdong 515063，China

[*]Corresponding authors

Contact: Dr. Xiaoyu Ji, xyji@stu.edu.cn

Abstract

Alzheimer's disease (AD) and epilepsy (EP) share a complex bidirectional relationship, yet the molecular mechanisms underlying their comorbidity remain insufficiently explored. To identify potential consensus transcriptional programs across animal models and human patients with AD and EP, we conducted comprehensive genome-wide transcriptomic analyses of multiple datasets. Our investigation included mouse models of temporal lobe epilepsy (pilocarpine- and kainic acid-induced; n = 280), mouse models of AD (7 transgenic models expressing human tau or amyloid pathology; n = 257), and performed cross-species validation in human cohorts (EP: n = 182; AD: n = 301). Our unsupervised gene co-expression analysis revealed a highly conserved immune-related module across all models and patient cohorts. The hub consensus signatures of this module were centered around a microglial synaptic pruning pathway involving *TYROBP*, *TREM2*, and *C1Q* complement components. Gene regulatory network analysis identified *TYROBP* as the key upstream hub signature. These hub consensus signatures showed consistent upregulation in both AD and EP human bulk and single-nucleus datasets, preserved their regulatory relationship across species, and demonstrated strong diagnostic value. Computational modeling further demonstrates the asymmetric sensitivity of synaptic pruning to neural network dynamics. Loss of inhibitory synapses has a disproportionately greater impact on the excitation/inhibition (E/I) balance, shifting it toward hyperexcitation and increasing neural network synchronization. Our findings

support a mechanistic hypothesis that identifies microglial complement-mediated synaptic pruning as a conserved central pathway linking neurodegeneration to epileptogenesis and suggested that targeting this pathway may offer therapeutic benefits for AD and EP comorbidity.

Keywords: Alzheimer's disease, epilepsy, synaptic pruning, computational neuroscience, modeling, transcriptome, *TYROBP*, *TREM2*, *C1Q*

Graphic abstract

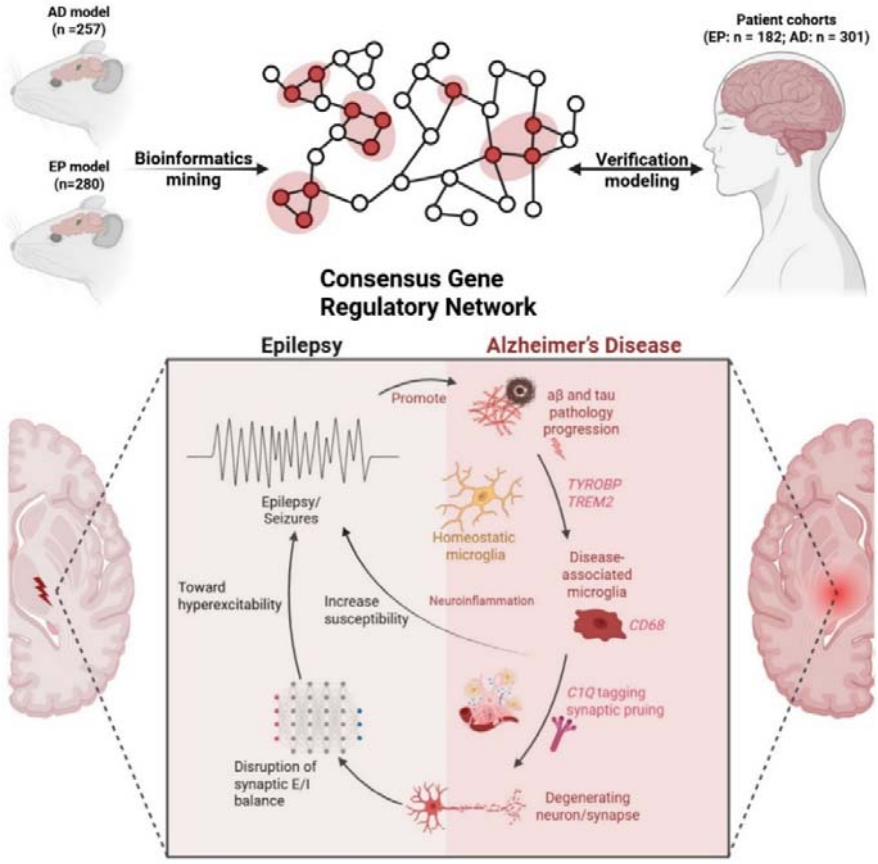

Highlights

- Genome wide transcriptomic analysis across epilepsy (EP) and Alzheimer's disease (AD) models and patients identified a conserved immune module.
- *TYROBP-TREM2-C1Q* microglial synaptic pruning pathway was identified as central consensus signature across model and patient datasets.
- Consensus transcriptional signatures showed strong diagnostic value in both AD and EP patient cohorts.
- Computational modeling demonstrates the asymmetric effects of synaptic pruning, whereby loss of inhibitory synapses disproportionately disrupts the E/I balance, leading to hyperexcitability and increased network synchronization.

1. Background

Alzheimer's disease (AD) and epilepsy (EP) are two common neurological diseases with a complex bidirectional relationship that contributes to their respective pathogenesis [1–3]. AD, characterized by progressive cognitive decline and neurodegeneration, is the leading cause of dementia worldwide, affecting an estimated 55 million individuals. This number is projected to triple by 2050 as life expectancy increases [4]. EP, characterized by recurrent unprovoked seizures, affects over 50 million individuals worldwide with a particularly high incidence among elderly populations, especially those with neurodegenerative conditions such as AD [5,6].

Epidemiological studies demonstrate a strong association between AD and EP. AD patients show increased susceptibility to EP, with 10–22% experiencing unprovoked seizures, while 22–54% demonstrating subclinical epileptiform activity during disease progression [7,8]. These seizures, predominantly occurring in the temporal lobe, correlate with accelerated cognitive decline and enhanced AD pathology [9]. Conversely, EP patients exhibit a two-fold higher risk of developing dementia compared to controls, with late-onset EP patients showing a three-fold increased risk [10,11]. This elevated risk is particularly evident in temporal lobe epilepsy (TLE), where numerous pathological features overlap with AD [9].

The pathological overlap between AD and EP extends across multiple biological levels [12]. At the molecular and cellular levels, both conditions feature amyloid deposition, tau accumulation, and hippocampal sclerosis—particularly evident TLE [13–15]. Chronic seizures increase neuronal activity and metabolic demands, potentially accelerating the production and aggregation of amyloid-β (Aβ) and hyperphosphorylated tau protein [16,17]. Conversely, the progressive accumulation of these pathological proteins in AD appears to lower seizure thresholds, promoting hyperexcitability and epileptiform activity [18,19]. At the network level, both disorders demonstrate profound disruption of the excitation/inhibition (E/I) balance, with a shift toward hyperexcitability driving both cognitive impairment and seizure susceptibility. This network dysfunction is accompanied by impaired synaptic plasticity, altered synchronization patterns, and progressive circuit reorganization [20–22].

Despite these established clinical and pathological connections, the precise molecular mechanisms governing the AD-EP relationship remain insufficiently explored. While previous studies have identified various potential contributors—including dysregulated protein homeostasis, mitochondrial dysfunction, and chronic inflammatory responses—most investigations have examined these conditions in isolation rather than specifically addressing their comorbidity [23–25]. Current research approaches have been limited by several factors: 1) inadequate integration of transcriptomic data across multiple disease models and human cohorts; 2) insufficient

attention to shared cellular processes that bridge molecular alterations with network dysfunction; and 3) limited application of computational modeling to connect molecular findings with clinically relevant physiological outcomes.

The challenge of treating EP in AD patients further underscores the need for deeper mechanistic insights. Clinicians face complex decisions regarding seizure treatment in AD patients, including whether to treat subclinical epileptiform activity and which antiseizure medications minimize cognitive side effects [26]. Emerging therapeutic approaches require more precise understanding of the shared pathological mechanisms. Systems biology and computational neuroscience approaches offer powerful tools to integrate insights from both animal models and human patients, potentially revealing actionable therapeutic targets that address both conditions simultaneously.

Emerging evidence suggests that AD and EP may share underlying molecular mechanisms. In this study, we investigated the hypothesis that consensus transcriptional programs exist across animal models and human patients with AD and EP. To test this, 1) we performed a genome-wide transcriptomic analysis of large-scale datasets from well-established mouse models of TLE (pilocarpine- and kainic acid-induced; n = 280) and AD (multiple transgenic models expressing human tau [TAU, rTg4510] or amyloid pathology [J20, TAS10, TPM, HO-TASTPM,

HET-TASTPM]; n = 257), aiming to identify robust, consensus transcriptional modules and signatures across distinct disease modeling paradigms, 2) cross-species validation of the diagnostic value of consensus transcriptional signatures and assessment of module preservation in human patient cohorts (EP cohorts: n = 182; AD cohorts: n = 301), 3) developed computational models to link molecular insights to network mechanisms of epileptogenesis. Our multi-cohort, cross-species analysis indicated strong, consensus transcriptional signatures centered on the microglial synaptic pruning pathway, which includes *TYROBP*, *TREM2*, and *C1Q* complement component. Computational modeling further suggests that neural network dynamics exhibit differential sensitivity to synaptic pruning, with inhibitory synapse loss having a more pronounced effect than excitatory synapse pruning. This asymmetric sensitivity drives network hyperexcitability and increased synchronization, potentially explaining the mechanistic link between AD and seizure susceptibility.

2. Materials and Methods

2.1 Data Collection

We conducted a comprehensive search to identify relevant transcriptomic datasets from both animal models and patient cohorts. The selection process involved screening based on sample size adequacy (n > 40) and research design to ensure statistical robustness and minimize bias. Our final selection comprised several

large-scale, methodologically sound datasets from both EP and AD research that focused on genome-wide expression patterns in well-characterized disease models and appropriate controls. We ultimately selected four large-scale datasets from animal models, along with three EP and two AD patient cohorts.

The EP model datasets included two of the most used TLE modeling approaches. The first dataset (PRJEB18790) contained 200 hippocampi of pilocarpine-induced (PO) model mice and wild-type (WT) controls [27]. The second dataset (GSE73878) comprised 80 hippocampal samples from the kainic acid-induced (KA) model and WT control. For the AD model datasets, we selected two datasets that systematically examined genome-wide expression alterations in amyloid and tau pathology progression. The Matarin dataset (GSE64398) contained 113 hippocampal samples from five mouse models and their controls: TAU mice, TAS10 mice, TPM mice, and TASTPM mice (both heterozygous and homozygous variants) [28]. The Castanho dataset (GSE125957) included J20 and rTg4510 models with 144 hippocampal and entorhinal cortex samples and matched controls [29]. To validate disease co-expression modules across species, we constructed modules using 129 hippocampal samples from TLE patients (GSE63808) and incorporated 30 consensus AD modules from the AMP-AD consortium's meta-analysis of 2,114 samples across seven brain regions [30,31]. To evaluate the diagnostic value of transcriptional signatures, we analyzed 47 hippocampal samples from TLE patients and controls (E-MTAB-3123), along with

253 samples from various brain regions of AD patients and controls (GSE48350). In addition, we reanalyzed single-nucleus RNA-sequencing (snRNAseq) datasets from TLE patients (cells = 66305) and AD cohorts (cells = 50985) to characterize cell-type-specific expression [32,33].

2.2 Quality control and preprocessing

All raw RNA sequences underwent quality control and trimming to obtain clean sequences, using FastQC (0.12.1) and Fastp (0.22.0) with stringent parameters (--qualified_quality_phred 30 --n_base_limit 5 --detect_adapter_for_pe --cut_tail --trim_front1 15 --dedup --trim_poly_x --trim_poly_g) to ensure high data quality [34]. Ribodetector (0.2.7) was used to remove potential rRNA contamination [35]. Low-quality regions in the reads (due to platform-specific artifacts) were also trimmed using Fastp. Trimmed sequences were then aligned to the GRCm39.111 reference mouse genome using HISAT2 (2.2.1) and followed by quantification using featureCounts (2.0.6) [36,37]. Detailed information on mapping metrics is provided in **Table S1**. Principal Component Analysis (PCA) and hierarchical clustering were performed to identify potential outlier samples. All datasets underwent appropriate normalization: RNAseq data were processed with variance-stabilizing transformation using DESeq2 (1.46.0), while microarray data were subjected to log2 transformation and variance-stabilizing normalization using the "limma" (3.62.1) package [38,39]. Batch effects were removed using limma:removeBatchEffect(). We assessed dataset

comparability by calculating general network properties such as average gene expression and overall network connectivity, with results indicating comparable across all datasets.

2.3 Gene Co-expression Networks Construction

To construct and compare gene co-expression networks (GCNs) between EP and AD model datasets, we implemented the standard WGCNA comparative methodology [40,41], which effectively identifies conserved gene modules across datasets while mitigating batch effects. Using the WGCNA package (1.73), we constructed signed co-expression networks in an unsupervised, unbiased manner based on genome-wide expression profiles. Network construction employed the minimum soft-thresholding power (β = 12) that achieved scale-free topology ($R^2 \geq 0.85$) across all model datasets. We generated adjacency matrices using the signed network option and transformed them into topological overlap matrices (TOM) to quantify gene connectivity profile similarities. Module identification proceeded through average linkage hierarchical clustering of TOM dissimilarity (1-TOM), followed by dynamic tree cutting (parameters: deepSplit = 1, minClusterSize = 27). For each module, we calculated module eigengenes (MEs) from the first principal component to summarize module expression profiles. We then identified disease-associated modules by computing Pearson correlation coefficients between MEs and genotype information, with significance thresholds of $P < 0.05$ and |correlation coefficient| > 0.35. Additionally,

we determined module membership (MM) and genotype significance (GS) by calculating Pearson correlations between individual genes and their respective MEs or genotypes. Gene Ontology (GO) enrichment analyses for module annotation were conducted using clusterProfiler (4.10.1) [42].

2.4 Module Preservation Analysis

To evaluate the preservation of EP model modules across AD model datasets, we implemented dual analytical approaches as described by Langfelder et al. [43]. First, we calculated Zsummary preservation statistics using the modulePreservation function (networkType = "signed", nPermutations = 100). This composite metric comprehensively assesses preservation by integrating module size, density, and connectivity parameters, quantifying how effectively EP module structures are maintained in AD datasets. We interpreted the preservation evidence according to established thresholds: strong (Zsummary > 10), moderate (2 < Zsummary < 10), or absent (Zsummary < 2). We complemented this analysis with the medianRank preservation statistic, which evaluates relative module preservation with reduced sensitivity to module size variations, where lower ranks indicate stronger preservation. Additionally, we performed cross-tabulation analysis to quantify module overlap between EP and AD model datasets, as well as between model and patient datasets. This approach generated contingency tables detailing the number of genes shared between reference and test dataset modules. We determined overlap significance

(adjusted $P < 0.05$) using Fisher's exact test with Benjamini-Hochberg (BH) correction for multiple testing.

2.5 Consensus Network and Signatures Identification

After confirming significant preservation of key modules across datasets, we constructed consensus modules to identify gene co-expression patterns consistently present in both conditions. This consensus approach involved calculating the component-wise minimum values of the topological overlap matrices from all datasets, thereby capturing shared network topology while filtering dataset-specific variations. We applied hierarchical clustering, using the same parameters as those applied to individual networks, to the consensus dissimilarity matrix (1-consensusTOM) to identify robust consensus modules [41]. Hub genes act as key drivers within a module and were identified using stringent criteria to minimize false positives: genes with MM > 0.9 and ranking in the top 5% for intramodular connectivity within each module. Consensus hub signatures were determined by intersecting the hub genes of key modules in both EP and AD datasets, requiring an overlap count of at least three across datasets. The expression and diagnostic value of these consensus hub signatures were further explored in the AD and EP patient datasets (GSE48350 and E-MTAB-3123).

To explore interactions and potential regulatory relationships among consensus hub

signatures, we constructed a protein-protein interaction (PPI) network using the STRING database (12.0) (https://string-db.org/cgi/input.pl) with a confidence score threshold of 0.4 and a false discovery rate (FDR) of 5% [44]. We also performed regulatory network analysis with the GENIE3 (1.28.0) algorithm, which applies a random forest approach to infer potential regulatory relationships from gene expression data. GENIE3 ranks regulatory interactions by weight, with higher weights indicating stronger regulatory links [45]. Gene expression profiles of the consensus hub signatures from all datasets were used to infer plausible regulatory interactions. To reduce false positives, only the top 30% plausible regulatory links were retained to construct gene regulatory networks.

2.6 Machine Learning

To evaluate the diagnostic potential of consensus hub signatures, we conducted binary classification (disease vs. control) across datasets using these signatures as predictive features. Prior to analysis, gene expression values underwent standardization to ensure comparable scaling across genes. We implemented classification models in Python 3.8.20 using scikit-learn, XGBoost, and CatBoost libraries. Seven supervised learning algorithms were evaluated: Logistic Regression (with increased maximum iterations of 1000), Support Vector Machine with RBF kernel, Random Forest, Naive Bayes, XGBoost, AdaBoost, and CatBoost. To ensure robust performance estimation and prevent overfitting, we employed 5-fold stratified cross-validation, with each fold

maintaining proportional representation of disease and control samples. Performance was assessed through multiple metrics including Accuracy, Precision, Recall, F1 score, and Area Under the Receiver Operating Characteristic Curve (AUC). The AUC was calculated by pooling predicted probabilities from all cross-validation splits to generate Receiver Operating Characteristic (ROC) curves.

2.7 Cell Composition Deconvolution and Single-nucleus RNA-seq Analysis

In silico deconvolution can estimate the cellular composition of a tissue sample from its bulk gene expression profile, with CIBERSORT particularly suited for cellular composition deconvolution of brain transcriptomes [46,47]. Cell composition deconvolution was performed using CIBERSORT (1.04**)** via the BrainDeconvShiny platform, with cell-type signatures specific to *Mus musculus* from immunopurified mouse brain tissue [46,47]. Associations between identified cell types and modules were determined by calculating Pearson correlation coefficients.

snRNA-seq datasets from EP and AD cohorts were reanalyzed to investigate cell-type-specific transcriptional changes of consensus transcriptional signatures. For EP cohort, we utilized snRNA-seq dataset (GSE190453) profiling temporal lobe tissue from TLE patients and non-epileptic controls (n = 8) [32]. For AD cohort, we analyzed snRNA-seq data from the Religious Orders Study and Rush Memory and Aging Project (ROSMAP) cohort, encompassing 48 prefrontal cortex (PFC) samples

from AD patients and non-pathology controls (n =48) [33]. Data preprocessing was performed using the Seurat package (5.0.1) according to the original studies [48]. Nuclei were filtered based on standard quality control criteria: nuclei with fewer than 200 detected genes, excessive gene counts (thresholds adjusted per sample), or mitochondrial transcript percentages exceeding 20% were excluded. Mitochondrial content was calculated using the PercentageFeatureSet() function. After filtering, SCTransform normalization was applied to each sample, regressing out total RNA counts and mitochondrial content to correct for technical variability. Batch correction across samples was performed via Seurat's integration workflow, anchoring on the top 3,000 variable features. Dimensionality reduction was conducted through PCA, with the first 30 components used for clustering and UMAP visualization. Cell-type annotation followed the definitions established in the original studies and calculate scores for each nucleus using the AddModuleScore() function, and cell-type identity was assigned based on the highest-scoring module. Cluster annotations were further refined by majority voting based on the predominant cell-type identity within each cluster. Differential expressions of consensus transcriptional signature between control and disease groups were evaluated using two-sided Wilcoxon rank-sum tests.

2.8 Computational modeling

We implemented a spiking neural network using the Izhikevich neuron model to simulate hippocampal CA3 circuit dynamics and explore the contribution of synaptic

pruning to pathological changes in AD and EP [49–51]. The network consisted of 1000 standard Izhikevich neurons (800 excitatory, 200 inhibitory) and simulated for 1000ms using the Brian2 package [52]. Network architecture included random sparse connectivity (0.1 probability) with conductance-based synapses modeling AMPA (excitatory) and GABA-a (inhibitory) currents across four connection types: E→E, E→I, I→E, and I→I [53]. Synaptic weights were drawn from a standard normal distribution and normalized to [0,1]. We simulated synaptic pruning by selectively removing excitatory or inhibitory synapses with the lowest weights (0-50%, with 5% increments), repeating each simulation at least 50 times.

To quantify network dynamics, we calculated the excitation/inhibition (E/I) ratio and event synchrony (ES) [54]. The E/I ratio compared total excitatory currents to the absolute magnitude of inhibitory currents, while ES measured spike timing coordination between excitatory neuron pairs within 5-ms windows. Both metrics were normalized to baseline unpruned values to reflect pruning-induced changes. Statistical analysis included Pearson correlation coefficients and linear regression to quantify the effect sizes of excitatory and inhibitory pruning on network dynamics. Complete details of the computational model parameters, equations, and analysis methods can be found in **Text S1.**

3. Results

3.1 Identification of Consensus Gene Co-Expression Network and Hub Signatures

To identify conserved molecular signatures underlying EP and AD, we employed an unbiased, genome-wide approach to construct GCNs across four independent datasets: two EP models (pilocarpine-induced [EP-PO] and kainic acid-induced [EP-KA]) and two AD datasets (AD-Castanho: [rTg4510, J20]; AD-Matarin: [TAU, TAS10, TPM, HO-TASTPM, HET-TASTPM]). After removing only genes with negligible or undetectable expression, we retained all expressed genes (ranging from 12,558 to 17,813) to avoid selection bias.

Network construction using consistent soft-thresholding power (β = 12) identified common and distinct GCNs modules across all model datasets (**Fig 1A, S1**): EP-PO revealed 19 modules (97- 1203 genes), EP-KA contained 14 modules (36-1534 genes), AD-Castanho yielded 28 modules (55-820 genes), and AD-Matarin showed 16 modules (33-1354 genes). Correlation analysis between module eigengenes and disease status identified disease-associated modules in each model (**Table S2**). In the EP-PO dataset, 12 modules showed significant association with the EP genotype ($|r| > 0.35$, $P < 0.05$). Similarly, EP-KA had 2 disease-associated modules, AD-Castanho contained 12 modules correlated with tau pathology, with 4 modules correlated with general AD pathology, and AD-Matarin revealed 5 modules associated with tau

pathology and 2 modules associated with amyloid pathology, with 3 modules correlated with general AD pathology (**Fig 1A, Table S2**).

Functional enrichment analysis of disease-specific modules revealed several distinct biological processes unique to each condition (**Table S2**). EP-specific modules were enriched in term such as "synapse organization" (PO-lightcyan), "modulation of chemical synaptic transmission" (PO-yellow) and "regulation of calcium ion import" (KA-midnightblue) while AD-specific modules showed enrichment in term such as "establishment of protein localization to organelle" (Matarin-blue), "dendrite development "(Castanho-saddlebrown) reflecting the unique pathophysiological mechanisms in each disease (**Table S2**). Despite disease-specific differences, cross-condition preservation analysis revealed remarkable conservation of an immune module across all four models (**Fig. 1A**). Using Z-summary preservation statistics and cross-tabulation approaches, we identified a large immune-related module (turquoise) with exceptionally highest preservation (Z-summary > 50) across all pairwise comparisons (**Fig. 1A, Table S2**). This module demonstrated significant overlap among all four models (adjusted P < 1E-300) and was negatively correlated neuron proportion and positively correlated with disease progression genotype in each model (**Table S2**): EP-PO (r = 0.80, P = 6.13E-42), EP-KA (r = 0.52, P = 9.31E-07), AD-Castanho (r =0.46, P = 8.63E-08), and AD-Matarin (r = 0.56, P = 9.14E-11).

The strong preservation pattern of this immune module across both diseases prompted us to construct consensus GCNs by integrating network topology information from all datasets (**Fig. S2**). This approach identified a robust immune-related and disease-associated consensus module containing 1617 genes common to all models (**Table S2-3**). To identify key drivers within this consensus immune module, we applied stringent criteria based on intramodular connectivity and module membership across all four datasets, which identified 19 consensus hub signatures consistently present in the immune modules across all models (**Fig. 1B**). These hub signatures included microglial activation markers (*TREM2, TYROBP, CD68*), *C1Q* complement components (*C1QA, C1QB, C1QC*), and inflammatory mediators (*TLR2, FCGR2B, CYBA*). Additional immune-related genes comprised lysosomal enzymes (*CTSH, CTSZ, GUSB*), immune signaling regulators (*CD84, CD52, SLC11A1, UNC93B1*), genes involved in phagocytosis and motility (*MYO1F, PROS1*), and the immune checkpoint receptor *LAG3*.

To investigate the biological significance and potential regulatory relationships among these hub signatures, we employed a multi-layered network analysis approach combining protein-protein interaction data from STRING with gene regulatory networks inferred by GENIE3 (**Fig. 1B**). Network centrality analysis identified *TYROBP* as the most upstream hub signature with highest total degree (regulator/target ratio = 1.33, total degree = 24.19), followed by *CD68, TREM2, C1Q*

complement components and *SLC11A1* (**Fig. 1B, Table S2**). GO enrichment analysis of the hub signature network identified "synaptic pruning" as the most significantly enriched biological process with strongest signal (FDR = 4.02E-07, signal = 2.91), which include *C1Q* complement components and microglial receptors (*TREM2*) (**Fig. 1C**). Genes involved in “Synaptic pruning” also participate in other enriched processes such as “Complement-mediated synapse pruning” (*C1QA*, *TREM2*) and “Microglial cell activation” (*TYROBP*, *C1QA*, *TREM2*, *SLC11A1*, *TLR2*) (**Fig. 1C, Table S2**).

Taken together, our genome wide transcriptomic analysis revealed a highly conserved immune module in EP and AD model, with a consensus regulatory network centered around *TYROBP*, *TREM2*, *CD68*, *C1Q* components that coordinate microglia activation and synaptic pruning. This consensus molecular pathway represents a potential central mechanism linking both neurological conditions.

3.2 Consensus GCNs Significantly Overlap with GCNs in Human Patients

To validate the translational relevance of our identified consensus GCNs, we compared them with disease-associated GCNs from human patient datasets. We employed a comprehensive cross-species approach to identify overlaps between our consensus modules and published AD-associated co-expression modules from 2,114 samples across seven brain regions, as well as our newly constructed EP patient

modules from 127 TLE patient hippocampal samples (**Fig. 2A, S3, Table S3**).

Our analysis revealed significant overlaps between the consensus immune module and multiple human AD modules across different brain regions. The strongest associations were observed with modules from cerebellum (CBE), dorsolateral prefrontal cortex (DLPFC), and superior temporal gyrus (STG) regions. The consensus module demonstrated particularly strong overlap with the " CBE-turquoise" module (n = 502 genes, 25.39% of the patient module, P < 1E-300), the "DLPFC-blue" module (n = 502 genes, 28.67% of the patient module, P < 1E-300) and "STG-blue"(n = 389 genes, 33.22% of the human module, P < 1E-300) (**Fig. 2A, Table S2**). Similarly, substantial overlaps were detected with modules from inferior frontal gyrus (IFG), superior temporal gyrus (STG), temporal cortex (TCX), and frontal pole (FP) but the overlap percentage varied from 2% to 33% (**Table S2**).

For EP patient dataset, our consensus module showed significant overlap with two EP patient's co-expression modules (yellow: n = 153 genes, 39.64% of the patient module, P < 7.07E-88; blue: n = 279 genes, 22.85% of the patient module, P < 1.06E-84) (**Fig. 2A, Table S2**). Notably, the top hub genes identified in our animal model analysis—*TYROBP*, *TREM2*, and the *C1Q* components—were also identified as central hub genes in the corresponding EP patients's yellow module, with *TYROBP* showed the top 2 intramodular connectivity (**Table S3**).

To further validate our hub consensus signatures findings, we examined whether the 19 previously identified hub signatures remained clustered within the same modules in human disease networks (**Fig. 2B**). The co-occurrence analysis revealed strong co-expression patterns, with particularly strong co-expression observed among *C1Q* complement components, *TREM2*, *TYROBP*, *CYBA*, *SLC11A1*. These genes showed the highest co-occurrence frequency (dark blue in the heatmap), suggesting they function as a coordinated unit across species and disease conditions. Collectively, these cross-species analyses demonstrate that the identified immune modules and hub signatures represent conserved biological entities relevant to both AD and EP pathogenesis in humans.

3.3 Consensus Hub Signatures Displayed Strong Diagnostic Value

To validate the clinical relevance of the identified consensus hub transcriptional signatures in AD and EP animal models, we analyzed the expression of 19 hub consensus signatures in bulk and single nucleus datasets from AD and EP patients (GSE48350, E-MTAB-3123, GSE190453 and ROSMAP PFC) compared to their controls.

Firstly, we localized the expression of these signatures in patient cell types, which demonstrated predominantly expression in microglia (**Fig. 3A-D**). Some signatures

such as *CTSH*, *MYO1F*, and *GUSB* showed broad expression across various cell types. Among all the microglia-specific signatures, expression of *TYROBP*, *TREM2*, and the *C1Q* complement genes were consistently detectable and exhibited high average expression across EP and AD cohorts (**Fig. 3B, D**). We then performed differential expression analysis on microglia and bulk datasets (**Fig. 3E-H**). We observed that almost all signatures were significantly upregulated in the EP cohort, and most signatures were also significantly upregulated in the AD cohort, with particularly high expression in microglia of late pathology (**Fig. 3G**). Notably, *TYROBP*, *TREM2*, and the *C1Q* complement genes—identified as central consensus signatures implicated in microglial synaptic pruning—were consistently upregulated in both disorders (**Fig. 3E-H**).

Using these gene expression profiles from bulk datasets (GSE48350, E-MTAB-3123), we developed diagnostic models with multiple machine learning algorithms to explore the diagnostic value of these 19 hub consensus signatures. These models generally achieved excellent discrimination in the EP dataset (AUC > 0.9) and good performance in the AD cohort (AUC > 0.7) (**Fig. S4**). The superior classification accuracy in EP likely reflects the more substantial transcriptional alterations observed in these patients. These findings demonstrate that these consensus signatures also dysregulated in human patients and possess strong diagnostic utility. This is especially true for genes involved in microglia activation and synaptic pruning (e.g., *TYROBP*,

TREM2, and the *C1Q* complement genes).

3.4 Asymmetric Effects of Synaptic Pruning on Neural Network Dynamics

To better understand how synaptic pruning influences neural network dynamics and its potential role in the comorbidity of AD and EP, we developed a neural network model simulating the hippocampal CA3 circuit. In this model, we systematically varied the extent of synaptic pruning (0% to 50%) at either excitatory or inhibitory synapses. We then quantified changes in the E/I ratio and synchronization levels, conducting at least 50 simulation runs per condition (**Fig. 4**).

Our findings indicate that pruning either excitatory or inhibitory synapses alters the E/I ratio, but with differential effects. Inhibitory synaptic pruning significantly elevated the E/I ratio, while excitatory pruning reduced it. These bidirectional trends were consistent across all simulations and in experiments where excitatory or inhibitory pruning was varied independently (**Fig. 4A**). Correlation analysis revealed a negative association between excitatory pruning and the E/I ratio ($r = -0.474$) and a stronger positive correlation between inhibitory pruning and the E/I ratio ($r = 0.684$) (**Fig. 4B**). Linear regression further confirmed this differential sensitivity, with excitatory pruning reducing the E/I ratio ($\beta = -1.038$), whereas inhibitory pruning increased more substantially ($\beta = 1.454$), indicating that E/I balance is more sensitive to changes in inhibitory connectivity (**Fig. 4B**).

Notably, network synchronization exhibited an even more pronounced differential sensitivity to pruning type. Inhibitory pruning displayed a moderate positive correlation with event synchronization (r = 0.346), while excitatory pruning showed only a negligible negative correlation (r = −0.039) (**Fig. 4B**). Linear regression analysis further confirmed this asymmetric sensitivity, with inhibitory pruning exerting a substantially stronger effect on synchronization (β = 0.358) compared to excitatory pruning (β = −0.041) (**Fig. 4B**). Additionally, the E/I ratio itself was positively correlated with synchronization (r = 0.491), suggesting that the influence of synaptic pruning on network synchronization may be indirectly mediated through its effects on E/I balance (**Fig. 4C**).

These simulations demonstrate that while both types of synaptic pruning affect network properties, inhibitory pruning exhibits a heightened potency in disrupting both E/I balance and synchronization dynamics. This differential sensitivity to inhibitory pruning may represent a key mechanism by which synaptic loss in neurodegeneration conditions could precipitate network hyperexcitability and hypersynchrony characteristic of epileptiform activity.

4. Discussion

While Alzheimer's disease (AD) and epilepsy (EP) share a complex bidirectional

relationship, the molecular pathways linking AD-related neurodegeneration to increased EP susceptibility remain insufficiently explored. To address this gap, we employed robust genome-wide, unsupervised bioinformatic and computational approaches to analyze transcriptional data from multiple large-scale animal models and human patient datasets. This comprehensive analysis identified consensus molecular pathways, cellular processes, and neural network dynamics associated with this comorbidity across diverse experimental paradigms.

Conserved Neuroinflammation Pathways in Epilepsy and Alzheimer's Disease

Our genome-wide analysis provides compelling evidence supporting the hypothesis that neuroinflammatory pathways form a common molecular substrate between AD and EP [55]. We identified remarkable preservation of the immune-related turquoise module across both disease models and human patient datasets **(Fig. 1-2**). Functional enrichment analysis of the preserved module revealed significant enrichment in neuroinflammatory processes, such as "inflammatory response", "cytokine production", "blood vessel morphogenesis", "glial cell activation", and "complement and coagulation cascades" (**Table S2**).

Neuroinflammation has been extensively documented in both diseases and appears to serve a complex dual role in disease progression [55–57]. While activated microglia facilitate Aβ plaque clearance and reactive astrocytes provide metabolic support and

ionic homeostasis that may attenuate neural damage and seizures, chronic activation or dysfunction of these glial populations can promote disease progression through persistent neuroinflammation [58–60]. Specifically, activated microglia and astrocytes secrete proinflammatory cytokines and chemokines, including IL-1β, TNF-α, and IL-6, which can enhance neuronal hyperexcitability, increase seizure susceptibility, exacerbate Aβ and tau aggregation, and accelerate neurodegeneration and cognitive decline [61].

Additional inflammatory components, including complement cascade activation and blood-brain barrier (BBB) dysfunction, are implicated in both pathologies [62–65]. Complement activation contributes to synaptic loss in AD and is elevated in TLE patient tissue [64,65]. BBB disruption precedes neuronal hyperactivity in EP, promoting astrocyte dysfunction and seizures. In AD, BBB disruption facilitates peripheral inflammatory cell infiltration, thereby amplifying neuroinflammation [62,63].

These results establish neuroinflammation as a key mechanistic link between AD and EP [55]. AD-associated inflammation can enhance neuronal hyperexcitability and seizure susceptibility. Conversely, EP-induced inflammation may accelerate Aβ and tau accumulation, contributing to cognitive decline. Our results support previous studies and suggest that neuroinflammation is highly conserved across both diseases and species.

Synaptic Pruning was Identified as a Core Pathway in this Comorbidity

Our systematic in-depth analysis of the conserved immune module revealed a central synaptic pruning pathway involving *TYROBP*, *TREM2*, and *C1Q* complement genes (**Fig. 1**). These genes demonstrated consistent co-dysregulated in microglia and bulk expression data and demonstrated strong diagnostic value across both AD and EP patient, (**Fig. 2-3**). Collectively, these findings suggest that this microglia-mediated synaptic pruning may represent a core mechanistic pathway underlying the comorbidity of AD and EP.

This pathway has been extensively documented in AD pathology and experimental studies, demonstrating its involvement in both tau and Aβ pathology [66–69]. Dysregulation or mutations in *TYROBP* and *TREM2* are established risk factors for AD due to their effects on microglial function [70–72]. Under physiological conditions, microglia maintain synaptic homeostasis through a regulated process in which complement proteins, including *C1Q*, tag unnecessary synapses for elimination [73]. Microglial receptors, particularly *TREM2* and *TYROBP*, recognize these tags and initiate phagocytic clearance, a process critical for neural circuit refinement and maintenance in the adult brain [66]. In AD pathology, these receptors enable microglia to recognize protein deposits, triggering their transition to a disease-associated microglial (DAM) state characterized by enhanced phagocytic activity and elevated

expression of *TYROBP*, *TREM2*, *APOE*, and complement proteins including *C1Q* [66]. While *TYROBP* or *TREM2* deficiency disrupts DAM activation and impairs critical microglial functions such as plaque clearance, potentially accelerating AD pathology, overactivation of this pathway can also contribute to neurodegeneration and cognitive decline through excessive *C1Q*-mediated synaptic pruning [67–69].

Synaptic pruning can exert effects on both AD and EP disease progression through two primary mechanisms: synaptic transmission and synaptic plasticity. Regarding synaptic plasticity, research demonstrated that *C1Q* inhibition in aged experimental models can restore both long-term potentiation (LTP) and long-term depression (LTD) [67–69]. In non-aged models, increased *C1Q* expression also impairs the LTP process [74]. This is particularly relevant for AD, where impaired synaptic plasticity is a feature of cognitive decline. In EP, compromised synaptic plasticity may contribute to the formation and maintenance of epileptogenic circuits. Regarding synaptic transmission, elevated *C1Q* expression or Aβ accumulation in the CA1 region leads to decreased miniature and evoked excitatory postsynaptic currents [75,76]. In AD, this reduction in synaptic transmission contributes to cognitive decline by disrupting normal neural communication. For EP, this alteration affects both excitatory and inhibitory neurons [74], potentially contributing to the imbalance between excitation and inhibition that characterizes epileptic activity. Notably, these effects can be reversed through *C1Q* downregulation [77,78]. The relationship between these mechanisms appears

bidirectional: excessive synaptic pruning leads to neuronal damage and reduced LTP, which in turn promotes disease progression in both conditions, creating a harmful feedback loop where synaptic dysfunction promotes pathological processes.

Notably, interventions targeting the synaptic pruning pathway, whether through the knockdown of regulatory genes like *TYROBP* and *TREM2* or direct inhibition of *C1Q* accumulation, have successfully restored both electrophysiological and cognitive functions in AD models. This restoration occurred even in the presence of significant amyloid and tau pathology [66–69]. Our results establish a regulatory network that is consistent with previous observations and further extends its role in the comorbidity of AD and EP (**Fig. 1**).

While this pathway has been thoroughly investigated in AD pathology, to the best of our knowledge, no previous studies have linked it to the comorbidity between EP and AD. Additionally, our understanding of how synaptic pruning relates to EP remains limited, particularly regarding its effects on global neural network dynamics [79]. To address this gap, we conducted an in-silico experiment to shed light on this issue.

Asymmetric Effects of Synaptic Pruning Promote Network Synchronization

Computational modeling has become an important tool for understanding AD and EP pathology, with models ranging from molecular-level simulations of ion dynamics to

large-scale network models [80,81]. To explore how synaptic pruning contributes to the comorbidity of AD and EP, we developed a computational model of the hippocampal CA3 circuit building upon Liu's biologically plausible EP modeling framework [53]. This model allowed us to quantify how pruning of excitatory and inhibitory synapses affects E/I balance (E/I ratio) and the temporal coordination of neural firing (synchronization).

Our computational model reveals a differential sensitivity of neural networks to synaptic pruning, with E/I balance being substantially more responsive to inhibitory synapse loss than excitatory synapse elimination (**Fig. 4**). Quantitative analysis by linear regression demonstrated that excitatory synapse elimination decreased the E/I ratio (β = -1.038), while inhibitory synapse removal led to a significantly larger increase in the E/I ratio (β = 1.454) (**Fig. 4B**). This heightened sensitivity to inhibitory pruning can be explained by the architectural role of inhibitory interneurons within neural circuits. These neurons often establish synaptic connections with multiple excitatory neurons and act as crucial regulators of circuit coordination and synchronization. Therefore, when inhibitory control mechanisms are impaired, the resulting dysregulation cascades throughout more widespread circuits [82]. Consequently, a reduction in inhibitory synapses produces a disproportionately larger perturbation in neural networks than an equivalent reduction in excitatory synapses.

Even more striking was the asymmetric sensitivity of network synchronization to different types of synaptic pruning. Our findings reveal that inhibitory pruning exhibited a moderate positive correlation with synchronization (r = 0.346), whereas excitatory pruning had a negligible correlation (r = −0.039) (**Fig. 4B**). This differential sensitivity suggests that synchronization dynamics are primarily vulnerable to disruptions in inhibitory circuitry. Notably, the E/I ratio itself demonstrated a strong correlation with synchronization levels (r = 0.491) (**Fig. 4C**). While it seems intuitive that enhancing network excitability can promote synchrony, our analysis highlights the importance of considering the specific location and functional role of pruned synapses in neural circuits. For example, in a circuit that exerts an inhibitory effect on the broader network, pruning inhibitory synapses that inhibits this circuit paradoxically reduces network synchronization. This explains the indirect, nonlinear association of synaptic pruning with network synchronization.

Although establishing a direct causal relationship between synaptic pruning and AD-EP comorbidity remains challenging, our simulation results suggest a mechanistic pathway whereby neuronal or synaptic loss in neurodegenerative diseases disrupts E/I balance with heightened sensitivity to inhibitory synapse loss, thereby promoting EP susceptibility (**Fig. 4**). This mechanism may extend beyond AD, as EP is a well-documented comorbidity of multiple neurodegenerative conditions including Huntington's and Parkinson's disease[83]. Our simulations demonstrate that even with a

proportional loss of both synapse types (or even with greater excitatory synapse loss), the effect of inhibitory synapse loss can overpower that of excitatory synapse loss. This occurs due to differential sensitivity, leading to more extensive disruption of network E/I balance and promoting network synchronization (**Fig. 4**). Similar to *TYROBP* and *TREM2* being established risk factors for AD [71,72], Mendelian randomization studies have also indicated that *C1Q* a is a risk factor for both AD and EP (**Fig. S5**) [84]. Notably, in AD, synaptic loss often precedes cognitive decline and EP, suggesting it may be an initiating event rather than a consequence [1].

Our results emphasize the critical role of inhibitory synaptic pruning in promoting network synchronization due to the neural network's heightened sensitivity to inhibitory synapse loss. At the molecular level, *C1Q* functions as an "eat me" signal, tagging synapses for microglial elimination [79]. While this tagging process itself is not synapse-type specific, interestingly, several recent studies have demonstrated that microglia may preferentially prune inhibitory synapses [79,85]. Dejanovic et al. demonstrated that the *TREM2-C1Q* microglial synaptic pruning pathway engulfs inhibitory synapses more frequently than excitatory synapses in AD models, while Fan et al. observed similar preferential pruning of inhibitory synapses during recurrent seizures that exacerbate EP model pathology [85,86]. Studies have shown that *C1Q* blockade reduces both the frequency and severity of seizures in traumatic brain injury models [87]. However, it is also important to note that *C1Q* knockout also affects

synaptic elimination during development, resulting in enhanced connectivity and seizure activity [88,89]. Recently, Aloi et al. also reported that overactivation of microglia reduced Aβ pathology but also caused hyperexcitability and seizures via synaptic pruning [90].

These findings collectively suggest that the network's differential sensitivity to inhibitory synapse loss, coupled with the apparent preferential pruning of inhibitory synapses by microglia, may represent a critical mechanism underlying AD-EP comorbidity. The management of microglial *C1Q*-mediated synaptic pruning during AD pathology and aging warrants further investigation, particularly regarding the regulation of this potential preferential pruning of inhibitory synapses.

Limitations

Our study presents two key limitations. First, while we identified a conserved microglial synaptic pruning pathway across multiple datasets, our reliance on bulk expression data limits our ability to fully characterize microglial and neuron subtype-specific contributions. Despite our computational deconvolution efforts and cell type expression analyses, future research should employ spatial transcriptomics to more precisely map the cell subtype-specific dynamics in AD-EP comorbidity, particularly focusing on microglial activation patterns and their synaptic targeting behavior.

Second, our computational model is informative about synaptic pruning's impact on network dynamics. However, it needs to simplify several aspects of neural circuits, including network topology and dendritic complexity. Future modeling cam incorporate more detailed cellular mechanisms and circuit architectures to better capture the molecular progression of AD-EP comorbidity and the asymmetric effects of inhibitory versus excitatory synaptic pruning on network synchronization.

Conclusion

Our study involved a genome-wide analysis of large-scale transcriptomic datasets from multiple AD and EP animal models, as well as human patient cohorts, revealing a consensus molecular signature converging on microglial synaptic pruning. We identified a highly preserved immune-related co-expression module centered on the *TYROBP-TREM2-C1Q* complement pathway that is consistently upregulated across species and disease conditions. To facilitate module reuse and validation by the research community, we also developed and provided a web application (https://github.com/HuihongLi/OverlapModule) that enables researchers to test the overlap preservation of their own modules across our module. Importantly, our computational modeling demonstrates that neural networks exhibit differential sensitivity to synaptic pruning, with inhibitory synapse loss exerting disproportionately powerful effects on E/I balance and network synchronization

compared to excitatory synapse loss.

These findings illuminate a mechanistic link between neuroinflammation and network dysfunction in AD-EP comorbidity. The complement-mediated synaptic pruning pathway can provide a unifying framework that explains the bidirectional relationship between these conditions observed clinically. The asymmetric sensitivity of neural networks to inhibitory pruning—coupled with evidence that microglia preferentially target inhibitory synapses—creates a pathological loop that drives hyperexcitability and hypersynchrony. These findings suggest that targeting microglia–complement signaling may provide disease-modifying benefits by preserving inhibitory circuit integrity and preventing the onset of network hyperexcitability. Future research utilizing spatial transcriptomics and selective manipulation of complement pathways in specific microglial subpopulations will be crucial to validate this mechanism and develop targeted therapeutic strategies for patients suffering from AD, EP, or their comorbidity.

Abbreviations

EP	Epilepsy
AD	Alzheimer’s disease
E/I	Excitation/Inhibition
TLE	Temporal lobe epilepsy

Aβ	Amyloid-β
PO	Pilocarpine-induced
KA	Kainic acid-induced
GCNs	Gene co-expression networks
WT	Wild-type
PCA	Principal Component Analysis
BH	Benjamini-Hochberg
GO	Gene ontology
TOM	Topological overlap matrices
MEs	Module eigengenes
MM	Module membership
GS	Gene-genotype significance
PPI	Protein-protein interaction
FDR	False discovery rate
AUC	Area Under the Receiver Operating Characteristic Curve
ROC	Receiver Operating Characteristic
CBE	Cerebellum
DLPFC	Dorsolateral prefrontal cortex
STG	Superior temporal gyrus
IFG	Inferior frontal gyrus
TCX	Temporal cortex

FP	Frontal pole
SVM	Support vector machine
ES	Event synchrony
BBB	Blood-brain barrier
DAM	Disease-associated microglial
LTP	Long-term potentiation
LTD	Long-term depression
BP	Biological processes
ROSMAP	Rush Memory and Aging Project
snRNAseq	Single nucleus RNA-sequencing

Figures and legends

Figure 1. Identification of conserved immune-related GCNs and hub signatures

(A) Chord diagram showing module preservation across EP and AD models. Each segment represents a gene module identified in different datasets. Purple connections indicate statistically significant module overlap (Fisher's exact test, adjusted $P <$ 1E-300), with color intensity corresponding to significance level (-log10(padj)). Inner tracks display module correlations with disease status (red: positive correlation; blue: negative correlation) and neuron proportion.

(B) Integrated PPI and regulatory network of consensus hub signatures identified across all models. Nodes represent hub genes consistently present in the preserved

immune module, with node size proportional to total weighted degree. Solid lines indicate validated protein-protein interactions (STRING), dotted lines indicate computationally inferred gene regulation (GENIE3), with edge width reflecting interaction strength. Node color indicates regulator/target ratio, with red showing stronger regulatory potential.

(C) GO enrichment analysis of consensus hub signatures. Bar length corresponds to enrichment signal strength, color indicates significance level (FDR), and size reflects gene count within each category. Bars represent significantly enriched biological processes, with "Synaptic pruning" emerging as the most significant enriched process with highest signal.

Figure 2. Comparison of consensus modules with patient modules.

(A) The overlap between the consensus immune module and disease-associated GCNs from human patients. Peripheral nodes represent modules from different brain regions in AD and EP patient datasets. Line thickness indicates the number of overlapping genes between each patient module and the consensus module, with thicker lines showing stronger connections. Line color intensity corresponds to statistical significance (-log10(padj)), with red-orange hues indicating the highest significance levels. The significant associations (adjust $P < 0.05$) were observed with modules across brain regions in AD patients, and with yellow and blue modules in EP patients.

(B) Co-occurrence heatmap of the 19 identified consensus hub signatures across

human disease modules. Color intensity represents the frequency of gene co-expression (darker blue indicates higher co-occurrence counts).

Figure 3. Expression of consensus hub signatures in EP and AD patient cohorts.

(A-D) UMAP visualization and dot plot showing cell type-specific expression of consensus hub genes in EP patient samples **(A-B)** and AD patient samples **(C-D)**. Microglia show the highest expression of most hub genes, with *TYROBP*, *TREM2*, and *C1Q* complement genes exhibiting particularly strong expression.

(E-H) Differential expression analysis of consensus hub genes in microglia and bulk tissue from EP patients (**E-F**) and AD patients (**G-H**) compared to controls. Bar heights represent fold changes with statistical significance indicated (*$p < 0.05$, **$p < 0.01$, ***$p < 0.001$).

Figure 4. Asymmetric Effects of synaptic pruning on neural network dynamics.

(**A**) Simulation results of excitatory pruning ratio (0-0.5), inhibitory pruning ratio (0-0.5), E/I ratio, and synchronization. X-axis: Excitatory pruning ratio; Y-axis: Inhibitory pruning ratio; Z-axis: Average E/I ratio. Colors indicate average synchronization levels from dark purple (close to 1, indicating no change in synchrony) to yellow (indicating higher synchrony).

(B) The distribution of E/I ratio and synchronization values across different pruning levels. Each violin represents the distribution of values at a given pruning ratio (0–0.5

in 0.05 increments). Embedded boxplots display median and interquartile ranges. Overlaid dots represent individual simulation outcomes. Regression results (slope, p-value, and Pearson's r) are displayed in the upper right of each panel, indicating that inhibitory pruning has a stronger positive correlation with both E/I ratio and synchronization, while excitatory pruning shows weaker or negative correlations.

(C) The relationship between E/I ratio and synchronization across all simulation conditions. A positive correlation is observed, suggesting that changes in E/I balance mediate alterations in network synchrony. Regression statistics are displayed in the corner.

Legends of supplementary files

Text S1: Computational modeling details

Table S1: Summary of Quality Control and Mapping Statistics

Table S2: Statistics of Module Preservation and Functional Enrichment

Table S3. Module gene information

Figure S1. Construction of co-expression modules in model datasets.

(A) Scale independence and mean connectivity plots for different soft-thresholding powers across all four datasets (EP-PO, EP-KA, AD-Matarin, AD-Castanho). A power of 12 was selected as the minimum threshold that achieved scale-free topology

($R^2 \geq 0.85$) across all datasets. (B-E) Sample dendrograms and trait heatmaps showing hierarchical clustering of genes and resulting modules for (B) AD-Matarin, (C) EP-KA, (D) AD-Castanho, and (E) EP-PO datasets. Upper dendrograms show gene clustering, while lower heatmaps display module-trait relationships, with red indicating positive correlations and blue indicating negative correlations with disease status.

Figure S2. Dendrogram of the consensus network

Hierarchical clustering dendrogram of the consensus network constructed by integrating topological overlap matrices from all four datasets (EP-PO, EP-KA, AD-Matarin, AD-Castanho). The color band beneath shows consensus module assignments, while the heatmap displays module-trait associations across multiple model and disease conditions and age variables. This consensus approach identified robust co-expression patterns conserved across both AD and EP models.

Figure S3. Construction of co-expression module in EP patient datasets.

Dendrogram of gene modules identified in the EP patient dataset using hierarchical clustering and dynamic tree cutting based on TOM. (parameters: Soft-thresholding power of 7 ensuring a scale-free topology ($R^2 \geq 0.85$), deepSplit = 1, minClusterSize = 28).

Figure S4. ROC curves of diagnostic models using shared hub gene expression.

ROC curves for classifiers trained on (A) AD patient dataset (GSE48350) and (B) EP patient dataset (E-MTAB-3123). Multiple machine learning classifiers, including Logistic Regression, Support Vector Machine (SVM), Random Forest, Naive Bayes, XGBoost, AdaBoost, and CatBoost, were evaluated using 5-fold stratified cross-validation. Models were trained using standardized expression values of all consensus hub genes.

Figure S5: Forest plot of Mendelian randomization result from DMRdb.

Forest plot showing hazard ratios (HR) and 95% confidence intervals (CI) for associations between Alzheimer's disease subtypes, epilepsy, and *C1QA* http://www.inbirg.com/DMRdb/. Red dots represent point estimates for hazard ratios, and horizontal lines indicate 95% confidence intervals. p-values are shown for each association. Values greater than 1.0 indicate increased risk for the outcome.

Declarations

Ethics approval and consent to participate

Not applicable.

Consent for publication

Not applicable.

Availability of data and materials

The datasets analyzed during the current study are available in the National Center for Biotechnology Information (NCBI), European Nucleotide Archive (ENA), and Synapse under the following accession numbers: PRJEB18790, GSE125957, GSE73878, GSE64398, GSE63808, E-MTAB-3123, GSE48350, GSE190453, syn51758062.1.

Competing Interests

The authors declare that they have no known competing financial interests or personal relationships that could have appeared to influence the work reported in this paper.

Funding

This research was supported by the Young Scientists Fund of the National Natural Science Foundation of China (Grant Nos. 82201629) and the Guangdong Provincial Science and Technology Special Fund (Grant Nos. 210803136872196)

Authors' contribution

HL conceptualized the study, conducted the investigation, developed the methodology, performed formal analysis, and contributed to writing the original draft and

reviewing/editing the manuscript. ZX, YT, YY, and BL contributed to the investigation, performed formal analysis, and participated in writing the original draft and reviewing/editing the manuscript. SC JL contributed to writing the original draft and reviewing/editing the manuscript. JW was involved in conceptualization and contributed to writing the original draft and reviewing/editing the manuscript. MC, XL, YS, ZD, and MH contributed to the investigation and participated in reviewing/editing the manuscript. BH and NW conceptualized the study and contributed to writing the original draft and reviewing/editing the manuscript. XJ provided supervision, acquired funding, contributed to conceptualization, and participated in writing the original draft and reviewing/editing the manuscript. All authors read and approved the final manuscript.

Acknowledgments

The results published here are in whole or in part based on data obtained from the **AD Knowledge Portal**

Reference

1. Vossel, K. A. *et al.* Seizures and Epileptiform Activity in the Early Stages of Alzheimer Disease. *JAMA Neurol.* **70**, 1158–1166 (2013).
2. Palop, J. J. & Mucke, L. Epilepsy and Cognitive Impairments in Alzheimer Disease. *Arch. Neurol.* **66**, 435–440 (2009).

3. Fang, Y. *et al.* Alzheimer Disease and Epilepsy: A Mendelian Randomization Study. *Neurology* **101**, (2023).

4. Prince, M. *et al.* World Alzheimer Report 2015. The Global Impact of Dementia: An analysis of prevalence, incidence, cost and trends. (Alzheimer's Disease International, 2015).

5. Ngugi, A. K., Bottomley, C., Kleinschmidt, I., Sander, J. W. & Newton, C. R. Estimation of the burden of active and life-time epilepsy: A meta-analytic approach. *Epilepsia* **51**, 883–890 (2010).

6. Mendez, M. F. & Lim, G. T. H. Seizures in Elderly Patients with Dementia. *Drugs Aging* **20**, 791–803 (2003).

7. Leitner, D. *et al.* Similar brain proteomic signatures in Alzheimer's disease and epilepsy. *Acta Neuropathol. (Berl.)* **147**, 27 (2024).

8. Pandis, D. & Scarmeas, N. Seizures in Alzheimer Disease: Clinical and Epidemiological Data: Seizures in Alzheimer Disease. *Epilepsy Curr.* **12**, 184–187 (2012).

9. Tombini, M. *et al.* Temporal Lobe Epilepsy and Alzheimer's Disease: From Preclinical to Clinical Evidence of a Strong Association. *J. Alzheimers Dis. Rep.* **5**, 243–261 (2021).

10. Johnson, E. L. *et al.* Association Between Midlife Risk Factors and Late-Onset Epilepsy: Results From the Atherosclerosis Risk in Communities Study. *JAMA Neurol.* **75**, 1375–1382 (2018).

11. Stefanidou, M. *et al.* Bi-directional association between epilepsy and dementia. *Neurology* **95**, e3241–e3247 (2020).
12. Noebels, J. A perfect storm: Converging paths of epilepsy and Alzheimer's dementia intersect in the hippocampal formation. *Epilepsia* **52**, 39–46 (2011).
13. Gourmaud, S. *et al.* Alzheimer-like amyloid and tau alterations associated with cognitive deficit in temporal lobe epilepsy. *Brain* **143**, 191–209 (2020).
14. Tai, X. Y. *et al.* Hyperphosphorylated tau in patients with refractory epilepsy correlates with cognitive decline: a study of temporal lobe resections. *Brain* **139**, 2441–2455 (2016).
15. Nelson, P. T. *et al.* Hippocampal sclerosis in advanced age: clinical and pathological features. *Brain* **134**, 1506–1518 (2011).
16. Watts, M. E., Pocock, R. & Claudianos, C. Brain energy and oxygen metabolism: Emerging role in normal function and disease. *Front. Mol. Neurosci.* **11**, 396508 (2018).
17. Zou, Y. *et al.* Epileptic seizures induced by pentylenetetrazole kindling accelerate Alzheimer-like neuropathology in 5×FAD mice. *Front. Pharmacol.* **15**, 1500105 (2024).
18. Born, H. A. Seizures in Alzheimer's disease. *Neuroscience* **286**, 251–263 (2015).
19. Toniolo, S., Sen, A. & Husain, M. Modulation of Brain Hyperexcitability: Potential New Therapeutic Approaches in Alzheimer's Disease. *Int. J. Mol. Sci.* **21**, 9318 (2020).

20. Palop, J. J. *et al.* Aberrant Excitatory Neuronal Activity and Compensatory Remodeling of Inhibitory Hippocampal Circuits in Mouse Models of Alzheimer's Disease. *Neuron* **55**, 697–711 (2007).
21. Toniolo, S., Sen, A. & Husain, M. Modulation of Brain Hyperexcitability: Potential New Therapeutic Approaches in Alzheimer's Disease. *Int. J. Mol. Sci. 2020 Vol 21 Page 9318* **21**, 9318 (2020).
22. Targa Dias Anastacio, H., Matosin, N. & Ooi, L. Neuronal hyperexcitability in Alzheimer's disease: what are the drivers behind this aberrant phenotype? *Transl. Psychiatry* **12**, 1–14 (2022).
23. Liew, Y. *et al.* Neuroinflammation: A Common Pathway in Alzheimer's Disease and Epilepsy. *J. Alzheimer's Dis.* **94**, S253–S265 (2023).
24. Kalyvas, A.-C., Dimitriou, M., Ioannidis, P., Grigoriadis, N. & Afrantou, T. Alzheimer's Disease and Epilepsy: Exploring Shared Pathways and Promising Biomarkers for Future Treatments. *J. Clin. Med.* **13**, 3879 (2024).
25. Giorgi, F. S., Saccaro, L. F., Busceti, C. L., Biagioni, F. & Fornai, F. Epilepsy and Alzheimer's Disease: Potential mechanisms for an association. *Brain Res. Bull.* **160**, 107–120 (2020).
26. Bosco, F. *et al.* Antiseizure Medications in Alzheimer's Disease from Preclinical to Clinical Evidence. *Int. J. Mol. Sci.* **24**, 12639 (2023).
27. Srivastava, P. K. *et al.* Genome-wide analysis of differential RNA editing in epilepsy. *Genome Res.* **27**, 440–450 (2017).

28. Matarin, M. *et al.* A Genome-wide Gene-Expression Analysis and Database in Transgenic Mice during Development of Amyloid or Tau Pathology. *Cell Rep.* **10**, 633–644 (2015).

29. Castanho, I. *et al.* Transcriptional Signatures of Tau and Amyloid Neuropathology. *Cell Rep*. **30**, 2040-2054.e5 (2020).

30. Johnson, M. R. *et al*. Systems genetics identifies Sestrin 3 as a regulator of a proconvulsant gene network in human epileptic hippocampus. *Nat. Commun.* **6**, 6031 (2015).

31. Wan, Y.-W. *et al*. Meta-Analysis of the Alzheimer's Disease Human Brain Transcriptome and Functional Dissection in Mouse Models. *Cell Rep*. **32**, (2020).

32. Chen, Z.-P. *et al*. Lipid-accumulated reactive astrocytes promote disease progression in epilepsy. *Nat. Neurosci.* **26**, 542–554 (2023).

33. Mathys, H. *et al.* Single-cell transcriptomic analysis of Alzheimer's disease. *Nature* **570**, 332–337 (2019).

34. Chen, S., Zhou, Y., Chen, Y. & Gu, J. fastp: an ultra-fast all-in-one FASTQ preprocessor. *Bioinformatics* **34**, i884–i890 (2018).

35. Deng, Z.-L., Münch, P. C., Mreches, R. & McHardy, A. C. Rapid and accurate identification of ribosomal RNA sequences via deep learning. *Nucleic Acids Res*. **50**, e60 (2022).

36. Kim, D., Paggi, J. M., Park, C., Bennett, C. & Salzberg, S. L. Graph-based genome alignment and genotyping with HISAT2 and HISAT-genotype. *Nat.*

Biotechnol. **37**, 907–915 (2019).

37. Liao, Y., Smyth, G. K. & Shi, W. featureCounts: an efficient general purpose program for assigning sequence reads to genomic features. *Bioinformatics* **30**, 923–930 (2014).
38. Love, M. I., Huber, W. & Anders, S. Moderated estimation of fold change and dispersion for RNA-seq data with DESeq2. *Genome Biol.* **15**, 550 (2014).
39. Ritchie, M. E. *et al.* limma powers differential expression analyses for RNA-sequencing and microarray studies. *Nucleic Acids Res*. **43**, e47 (2015).
40. Miller, J. A., Horvath, S. & Geschwind, D. H. Divergence of human and mouse brain transcriptome highlights Alzheimer disease pathways. *Proc. Natl. Acad. Sci.* **107**, 12698–12703 (2010).
41. Langfelder, P. & Horvath, S. WGCNA: an R package for weighted correlation network analysis. *BMC Bioinformatics* **9**, 559 (2008).
42. Wu, T. *et al.* clusterProfiler 4.0: A universal enrichment tool for interpreting omics data. *The Innovation* **2**, (2021).
43. Langfelder, P., Luo, R., Oldham, M. C. & Horvath, S. Is My Network Module Preserved and Reproducible? *PLOS Comput. Biol.* **7**, e1001057 (2011).
44. Szklarczyk, D. *et al.* The STRING database in 2025: protein networks with directionality of regulation. *Nucleic Acids Res*. **53**, D730–D737 (2025).
45. Huynh-Thu, V. A., Irrthum, A., Wehenkel, L. & Geurts, P. Inferring Regulatory Networks from Expression Data Using Tree-Based Methods. *PLOS ONE* **5**,

e12776 (2010).

46. Newman, A. M. *et al.* Robust enumeration of cell subsets from tissue expression profiles. *Nat. Methods* **12**, 453–457 (2015).

47. Sutton, G. J. *et al.* Comprehensive evaluation of deconvolution methods for human brain gene expression. *Nat. Commun.* **13**, 1358 (2022).

48. Dictionary learning for integrative, multimodal and scalable single-cell analysis | Nature Biotechnology. https://www.nature.com/articles/s41587-023-01767-y.

49. Izhikevich, E. M. Simple model of spiking neurons. *IEEE Trans. Neural Netw.* **14**, 1569–1572 (2003).

50. Sammons, R. P. *et al.* Structure and function of the hippocampal CA3 module. *Proc. Natl. Acad. Sci.* **121**, e2312281120 (2024).

51. Vyleta, N. P., Borges-Merjane, C. & Jonas, P. Plasticity-dependent, full detonation at hippocampal mossy fiber–CA3 pyramidal neuron synapses. *eLife* **5**, e17977 (2016).

52. Stimberg, M., Brette, R. & Goodman, D. F. Brian 2, an intuitive and efficient neural simulator. *eLife* **8**, e47314 (2019).

53. Liu, Y., Grigorovsky, V. & Bardakjian, B. Excitation and Inhibition Balance Underlying Epileptiform Activity. *IEEE Trans. Biomed. Eng.* **67**, 2473–2481 (2020).

54. Penn, Y., Segal, M. & Moses, E. Network synchronization in hippocampal neurons. *Proc. Natl. Acad. Sci.* **113**, 3341–3346 (2016).

55. Liew, Y. *et al.* Neuroinflammation: A Common Pathway in Alzheimer's Disease and Epilepsy. *J. Alzheimers Dis.* **94**, S253–S265 (2023).

56. Vezzani, A., French, J., Bartfai, T. & Baram, T. Z. The role of inflammation in epilepsy. *Nat. Rev. Neurol.* **7**, 31–40 (2011).

57. Heneka, M. T., Golenbock, D. T. & Latz, E. Innate immunity in Alzheimer's disease. *Nat. Immunol.* **16**, 229–236 (2015).

58. Pekny, M. & Pekna, M. Astrocyte Reactivity and Reactive Astrogliosis: Costs and Benefits. *Physiol. Rev.* **94**, 1077–1098 (2014).

59. Chen, Z.-P. *et al.* Lipid-accumulated reactive astrocytes promote disease progression in epilepsy. *Nat. Neurosci.* **26**, 542–554 (2023).

60. Onyango, I. G., Jauregui, G. V., Čarná, M., Bennett, J. P. & Stokin, G. B. Neuroinflammation in Alzheimer's Disease. *Biomedicines* **9**, 524 (2021).

61. Vezzani, A. & Viviani, B. Neuromodulatory properties of inflammatory cytokines and their impact on neuronal excitability. *Neuropharmacology* **96**, 70–82 (2015).

62. van Vliet, E. A., Aronica, E. & Gorter, J. A. Blood–brain barrier dysfunction, seizures and epilepsy. *Semin. Cell Dev. Biol.* **38**, 26–34 (2015).

63. Zlokovic, B. V. Neurovascular pathways to neurodegeneration in Alzheimer's disease and other disorders. *Nat. Rev. Neurosci.* **12**, 723–738 (2011).

64. Kopczynska, M. *et al.* Complement system biomarkers in epilepsy. *Seizure* **60**, 1–7 (2018).

65. Veerhuis, R., Nielsen, H. M. & Tenner, A. J. Complement in the brain. *Mol.*

Immunol. **48**, 1592–1603 (2011).

66. Haure-Mirande, J.-V., Audrain, M., Ehrlich, M. E. & Gandy, S. Microglial TYROBP/DAP12 in Alzheimer's disease: Transduction of physiological and pathological signals across TREM2. *Mol. Neurodegener.* **17**, 55 (2022).

67. Haure-Mirande, J.-V. *et al.* Integrative approach to sporadic Alzheimer's disease: deficiency of TYROBP in cerebral Aβ amyloidosis mouse normalizes clinical phenotype and complement subnetwork molecular pathology without reducing Aβ burden. *Mol. Psychiatry* **24**, 431–446 (2019).

68. Haure-Mirande, J.-V. *et al.* Deficiency of TYROBP, an adapter protein for TREM2 and CR3 receptors, is neuroprotective in a mouse model of early Alzheimer's pathology. *Acta Neuropathol. (Berl.)* **134**, 769–788 (2017).

69. Audrain, M. *et al.* Integrative approach to sporadic Alzheimer's disease: deficiency of TYROBP in a tauopathy mouse model reduces C1q and normalizes clinical phenotype while increasing spread and state of phosphorylation of tau. *Mol. Psychiatry* **24**, 1383–1397 (2019).

70. Roussos, P. *et al*. The triggering receptor expressed on myeloid cells 2 (*TREM2*) is associated with enhanced inflammation, neuropathological lesions and increased risk for Alzheimer's dementia. *Alzheimers Dement.* **11**, 1163–1170 (2015).

71. Ma, J., Jiang, T., Tan, L. & Yu, J.-T. TYROBP in Alzheimer's Disease. *Mol. Neurobiol.* **51**, 820–826 (2015).

72. Jonsson, T. *et al.* Variant of TREM2 Associated with the Risk of Alzheimer's Disease. *N. Engl. J. Med.* **368**, 107–116 (2013).

73. Stevens, B. *et al.* The Classical Complement Cascade Mediates CNS Synapse Elimination. *Cell* **131**, 1164–1178 (2007).

74. Wu, X. *et al.* Complement C1q drives microglia-dependent synaptic loss and cognitive impairments in a mouse model of lipopolysaccharide-induced neuroinflammation. *Neuropharmacology* **237**, 109646 (2023).

75. Neniskyte, U. & Gross, C. T. Errant gardeners: glial-cell-dependent synaptic pruning and neurodevelopmental disorders. *Nat. Rev. Neurosci.* **18**, 658–670 (2017).

76. Hu, Y. *et al.* Wogonin mitigates microglia-mediated synaptic over-pruning and cognitive impairment following epilepsy. *Phytomedicine* **135**, 156222 (2024).

77. Bie, B., Wu, J., Foss, J. F. & Naguib, M. Activation of mGluR1 Mediates C1q-Dependent Microglial Phagocytosis of Glutamatergic Synapses in Alzheimer's Rodent Models. *Mol. Neurobiol.* **56**, 5568–5585 (2019).

78. Wu, J., Bie, B., Foss, J. F. & Naguib, M. Amyloid Fibril–Induced Astrocytic Glutamate Transporter Disruption Contributes to Complement C1q-Mediated Microglial Pruning of Glutamatergic Synapses. *Mol. Neurobiol.* **57**, 2290–2300 (2020).

79. Andoh, M., Ikegaya, Y. & Koyama, R. Synaptic Pruning by Microglia in Epilepsy. *J. Clin. Med.* **8**, 2170 (2019).

80. Yuan, P. *et al.* PLD3 affects axonal spheroids and network defects in Alzheimer's disease. *Nature* **612**, 328–337 (2022).

81. Stefanescu, R. A., Shivakeshavan, R. G. & Talathi, S. S. Computational models of epilepsy. *Seizure* **21**, 748–759 (2012).

82. Luo, L. Architectures of neuronal circuits. *Science* **373**, eabg7285 (2021).

83. Neri, S., Mastroianni, G., Gardella, E., Aguglia, U. & Rubboli, G. Epilepsy in neurodegenerative diseases. *Epileptic. Disord.* **24**, 249–273 (2022).

84. Zheng, X. *et al.* DMRdb: a disease-centric Mendelian randomization database for systematically assessing causal relationships of diseases with genes, proteins, CpG sites, metabolites and other diseases. *Nucleic Acids Res.* **53**, D1363–D1371 (2025).

85. Dejanovic, B. *et al.* Complement C1q-dependent excitatory and inhibitory synapse elimination by astrocytes and microglia in Alzheimer's disease mouse models. *Nat. Aging* **2**, 837–850 (2022).

86. Fan, J. *et al.* Preferential pruning of inhibitory synapses by microglia contributes to alteration of the balance between excitatory and inhibitory synapses in the hippocampus in temporal lobe epilepsy. *CNS Neurosci. Ther.* **29**, 2884–2900 (2023).

87. Holden, S. S. *et al.* Complement factor C1q mediates sleep spindle loss and epileptic spikes after mild brain injury. *Science* **373**, eabj2685 (2021).

88. Chu, Y. *et al.* Enhanced synaptic connectivity and epilepsy in C1q knockout mice.

Proc. Natl. Acad. Sci. **107**, 7975–7980 (2010).

89. Ma, Y., Ramachandran, A., Ford, N., Parada, I. & Prince, D. A. Remodeling of dendrites and spines in the C1q knockout model of genetic epilepsy. *Epilepsia* **54**, 1232–1239 (2013).

90. Aloi, M. S. *et al.* Microglia specific deletion of miR-155 in Alzheimer's disease mouse models reduces amyloid-β pathology but causes hyperexcitability and seizures. *J. Neuroinflammation* **20**, 60 (2023).

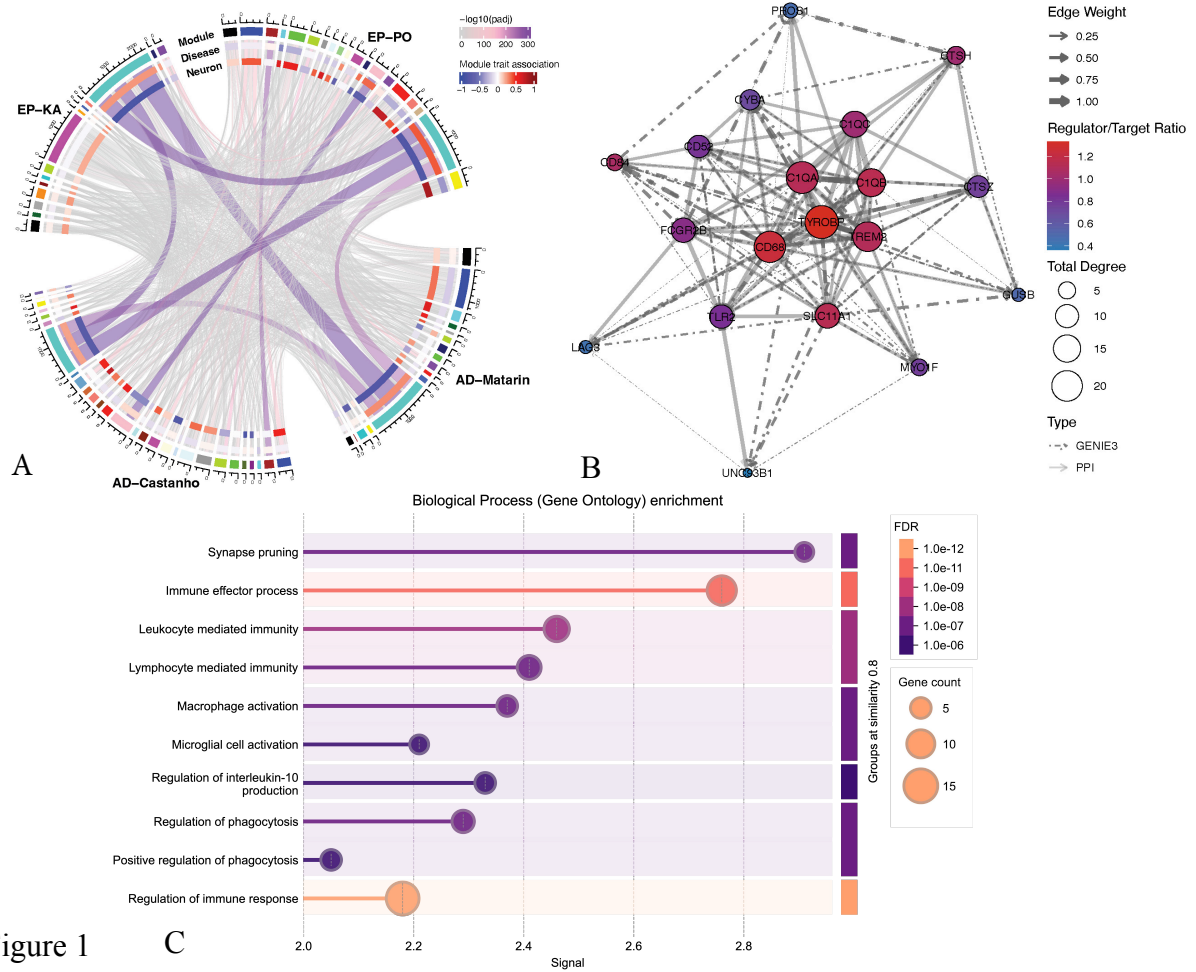

Module
Disease
Neuron
EP–PO
EP–KA
AD–Matarin
AD–Castanho
−log10(padj)
0 100 200 300
Module trait association
−1 −0.5 0 0.5 1
A
PROB1
GTSH
CYBA
C1QC
CD52
CD84
C1QA
C1QB
CTSZ
TYROBP
FCGR2B
TREM2
CD68
GUSB
TLR2
SLC11A1
LAG3
MYO1F
UNC93B1
B
Edge Weight
0.25
0.50
0.75
1.00
Regulator/Target Ratio
1.2
1.0
0.8
0.6
0.4
Total Degree
5
10
15
20
Type
GENIE3
PPI
Biological Process (Gene Ontology) enrichment
Synapse pruning
Immune effector process
Leukocyte mediated immunity
Lymphocyte mediated immunity
Macrophage activation
Microglial cell activation
Regulation of interleukin-10 production
Regulation of phagocytosis
Positive regulation of phagocytosis
Regulation of immune response
Groups at similarity 0.8
FDR
1.0e-12
1.0e-11
1.0e-09
1.0e-08
1.0e-07
1.0e-06
Gene count
5
10
15
2.0
2.2
2.4
2.6
2.8
Signal
C

Figure 1

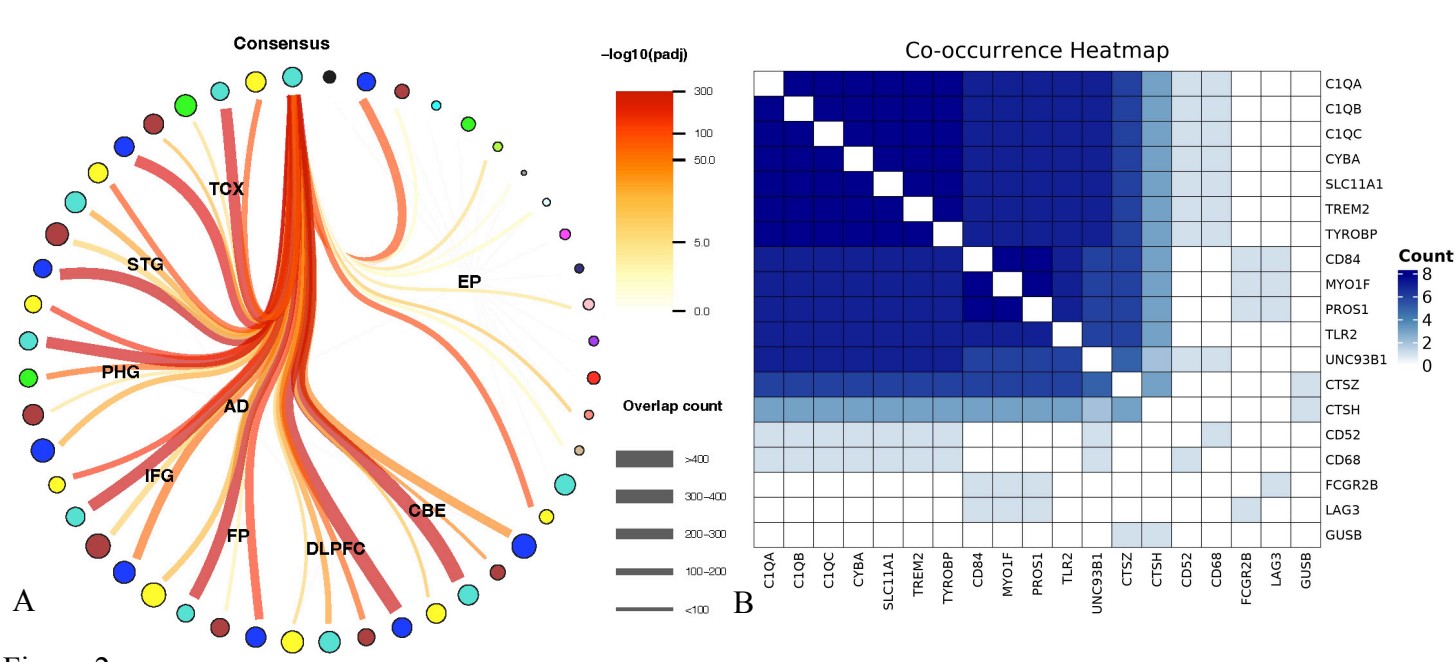
Consensus
TCX
STG
PHG
AD
IFG
FP
DLPFC
CBE
EP
A
−log10(padj)
300
100
50.0
5.0
0.0
Overlap count
>400
300–400
200–300
100–200
<100
Co-occurrence Heatmap
C1QA
C1QB
C1QC
CYBA
SLC11A1
TREM2
TYROBP
CD84
MYO1F
PROS1
TLR2
UNC93B1
CTSZ
CTSH
CD52
CD68
FCGR2B
LAG3
GUSB
Count
8
6
4
2
0
B

Figure 2

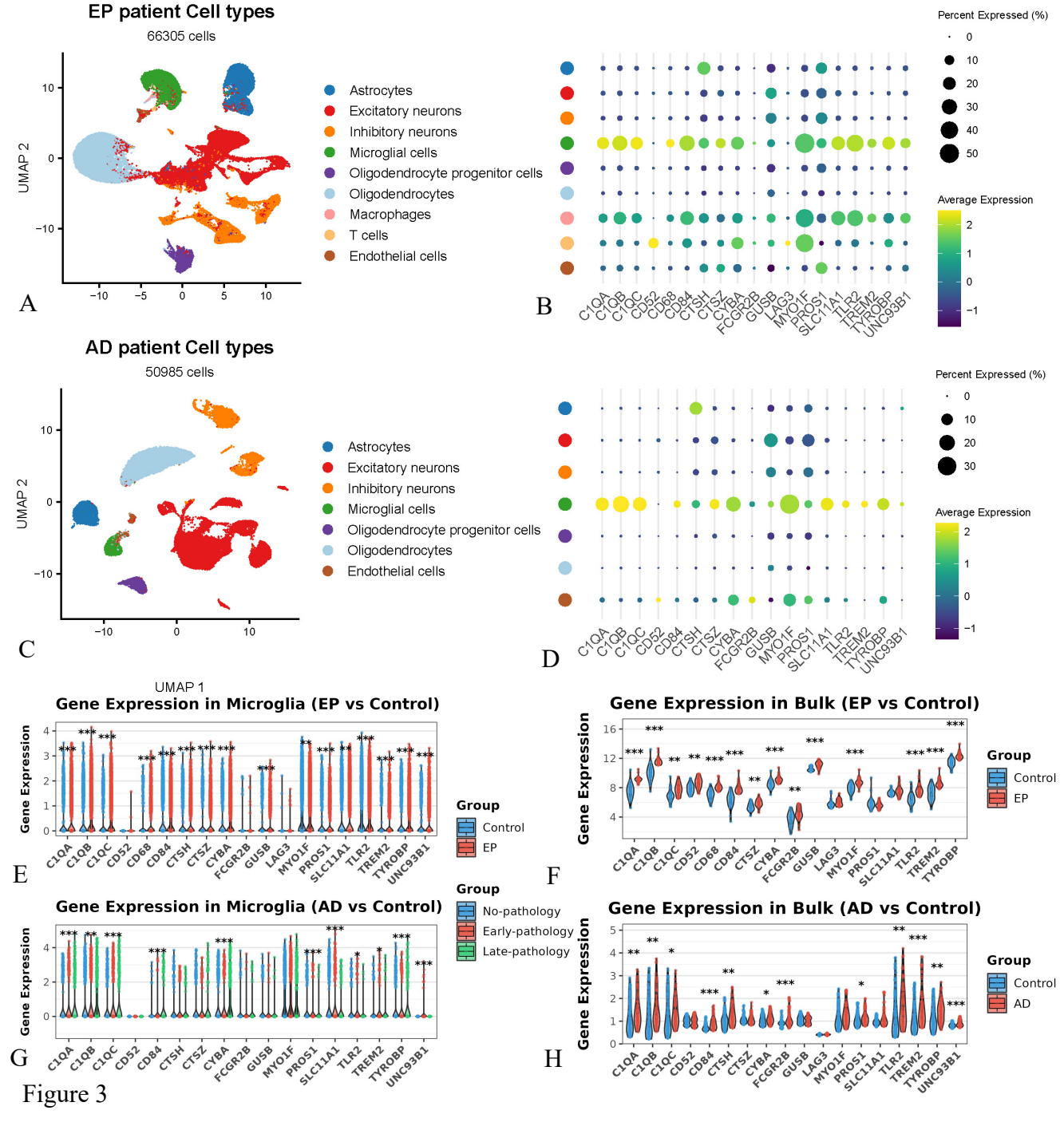
EP patient Cell types
66305 cells
UMAP 2
Astrocytes
Excitatory neurons
Inhibitory neurons
Microglial cells
Oligodendrocyte progenitor cells
Oligodendrocytes
Macrophages
T cells
Endothelial cells
A
Percent Expressed (%)
Average Expression
C1QA C1QB C1QC CD52 CD68 CD84 CTSH CTSZ CYBA FCGR2B GUSB LAG3 MYO1F PROS1 SLC11A1 TLR2 TREM2 TYROBP UNC93B1
B
AD patient Cell types
50985 cells
C
D
UMAP 1
Gene Expression in Microglia (EP vs Control)
Gene Expression
Group
Control
EP
E
Gene Expression in Bulk (EP vs Control)
F
Gene Expression in Microglia (AD vs Control)
No-pathology
Early-pathology
Late-pathology
G
Gene Expression in Bulk (AD vs Control)
AD
H

Figure 3

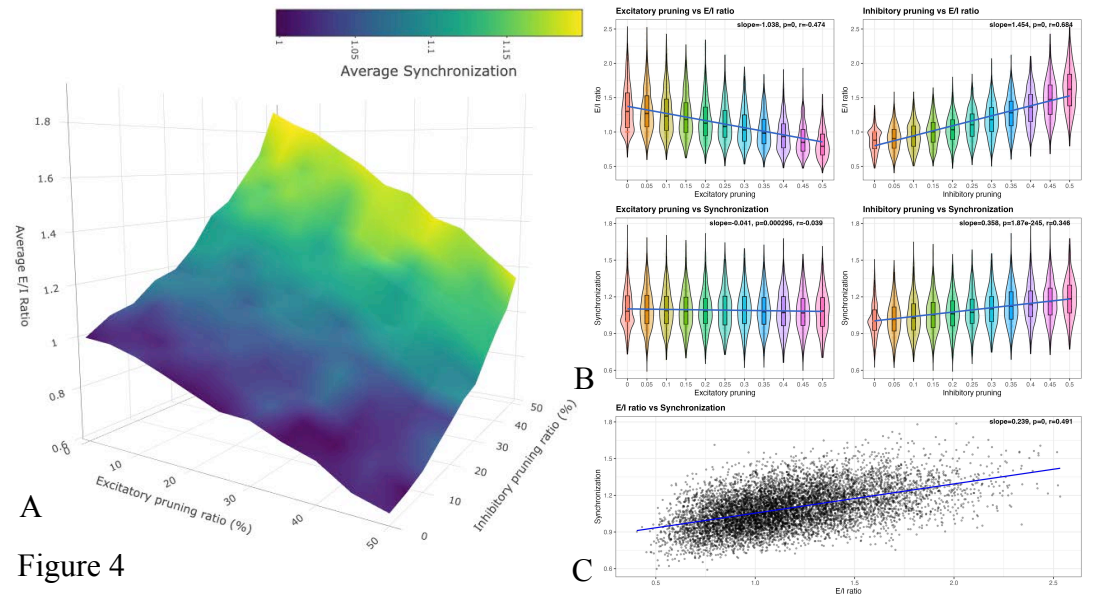
Average Synchronization
1
1.05
1.1
1.15
Average E/I Ratio
Excitatory pruning ratio (%)
Inhibitory pruning ratio (%)
A
Excitatory pruning vs E/I ratio
slope=-1.038, p=0, r=-0.474
Inhibitory pruning vs E/I ratio
slope=1.454, p=0, r=0.684
E/I ratio
Excitatory pruning
Inhibitory pruning
Excitatory pruning vs Synchronization
slope=-0.041, p=0.000295, r=-0.039
Inhibitory pruning vs Synchronization
slope=0.359, p=1.87e-245, r=0.346
Synchronization
B
E/I ratio vs Synchronization
slope=0.239, p=0, r=0.491
C

Figure 4